Effects of surface morphology and anisotropy on the tangential momentum accommodation coefficient between Pt(100) and Ar

T. Tung Pham, Quy-Dong To, Guy Lauriat, Céline Léonard, V. H. Vo

Effects of surface morphology and anisotropy on the Tangential Momentum Accommodation Coefficient between Pt(100) and Ar

Thanh Tung Pham, Quy Dong To,* Guy Lauriat, and Céline Léonard
Université Paris-Est, Laboratoire Modelisation et Simulation Multi Echelle, UMR 8208 CNRS, 5 Boulevard Descartes, 77454 Marne-la-Vallée Cedex 2, France

Vo Van Hoang
Department of Physics, Institute of Technology, National University of HochiMinh City, 268 Ly Thuong Kiet Street, District 10, HochiMinh City-Vietnam

(Dated: October 30, 2012)

In this paper, we study the influence of Platinum (100) surface morphology on the Tangential Momentum Accommodation Coefficient with Argon using Molecular Dynamics method (MD). The coefficient is computed directly by beaming Ar atoms into the surfaces and measuring the relative momentum changes. The wall is maintained at a constant temperature and its interaction with the gas atoms is governed by the Kulginov potential. To capture correctly the surface effect of the walls and atoms trajectory, the Quantum Sutton-Chen multi-body potential is employed between the Pt atoms. Effects of wall surface morphology, incident direction and temperature are considered in this work and provide full information of gas-wall interaction.

PACS numbers: 47.45.Gx, 47.11.Mn

I. INTRODUCTION

In most applications concerning a fluid flowing past a solid surface, the no-slip conditions are usually employed: the fluid velocity at the wall is assumed to be the same as the surface velocity. This assumption, which works well in many practical problems, breaks down when the channel height in consideration is at micro/nano length scale [1]. For gases, Maxwell introduced a gas-wall interaction parameter, the Tangential Momentum Accommodation Coefficient σ, to quantify the slip effects [2]. He postulated that after collision with the wall, a gas atom rebounds either diffusively or specularly, with the associated portions of σ and $(1-\sigma)$, respectively. The slip velocity, v_s, equal to the difference between the gas velocity at the wall and the wall velocity, can be evaluated by the following expression

$$v_s = \left(\frac{2-\sigma}{\sigma}\right)\lambda \left.\frac{\partial v}{\partial z}\right|_w \qquad (1)$$

where λ is the mean free path and $\left.\frac{\partial v}{\partial z}\right|_w$ is the derivative of the gas velocity at the wall surface. The latter is assumed to be normal to the z direction. Although Molecular Dynamics simulations showed that the reflection mechanism is more complicated than Maxwell's postulate, the coefficient σ is still widely used due to its simplicity. In practice, a fully accommodated coefficient, $\sigma = 1$, is frequently used whereas experiments record smaller values ranging from 0.7 to 1.0 and MD simulations results are even much smaller [3].

Based on Eq. (1), the σ parameter for a gas-wall couple can be determined by either experiments [4] or Molecular Dynamics [5, 6] in the Navier Stokes slip regime. However, most MD simulations of flows were done at nanoscale [7] and did not have the same conditions as in experiments. In order to compare calculations with measurements for dilute gases, a more relevant MD approach [8, 9] consists in studying every single gas-wall collision event. Consequently, σ can be computed directly by projecting gas atoms into the surfaces and finding momentum changes [10]. This approach, which is quite similar to beam experiments [11], provides insights into the reflection mechanism and can be used to improve Maxwell's model. As far as multi-scale simulations are concerned, the obtained fluid-wall interaction results can be coupled with other numerical methods [12–17].

We note that the term $\left(\frac{2-\sigma}{\sigma}\right)\lambda$ in (1) is equivalent to the slip length in Navier slip boundary conditions and the use of one parameter σ as in Maxwell's model means that the slip behavior is isotropic. For anisotropic textured surfaces, more sophisticate models are needed to reproduce the direction dependent slip or gas-wall interaction behavior. Bazant and Vinogradova [18] suggested using a slip length tensor to quantify this behavior. The tensorial nature of the slip effect was shown to be related to the interfacial diffusion [18–21]. Effective slip tensors with bounds for flows over superhydrophobic surfaces were also obtained [22, 23]. As the slip models describe macroscopic behaviors, it is thus relevant to investigate the problem at the scale of fluid wall interaction. For gases, Dadzie and Meolans [24] generalized Maxwell's scattering kernel by using anisotropic accommodation coefficients. The consequences of the model on the slippage have not been studied. Since the anisotropic scattering kernel model does not provide full information

* quy-dong.to@univ-paris-est.fr

about the gas-wall collisions, we shall use MD method to study these interactions in detail with the focus on the surface morphology. The MD code used in this paper is the parallel version described in Ref. [8]. The original code [25] has been enriched (e.g multi-body potentials, statistical tools, etc..) to adapt to the aim of the present work. The trajectory images are obtained by the molecular visualization program VMD [26].

Generally, results obtained from MD simulations depend on the following factors:
- The interaction potential between the gas/wall atoms.
- The dimension of the simulation models. In general, 3D models are better than 2D since it accounts for interactions of the gas atom with all its neighbors.
- The potential between the solid atoms must be good enough to reproduce the free surface effect. It is well known that the distance between the atomic layers near the free surface are much smaller than in the bulk.
- The temperature effect must be considered as gas molecules are adsorbed easier at cold walls than at hot walls, which can results in a higher σ.
- The surfaces are not always ideally smooth and can have different morphology (e.g randomly rough or textured surfaces).

This work aims at including these features in simulations of molecular beam experiments. The gas/wall couple under consideration is Argon and Platinum but the methodology of the present work can be used to obtain σ for any gas/wall couple provided that an appropriate potential is used. The paper is organized as follows. After the Introduction, Section 2 is devoted to the description of the computational method. It discusses briefly the choice of potentials, the method to prepare surface samples and MD simulation of gas/wall interaction. We remark that a part of surface sample preparation requires a separate molecular dynamics simulation of film deposition processes in order to create a realistic random roughness surface. The σ results issued from the calculations are then shown in Section 4. Finally, conclusions and perspectives are discussed.

II. COMPUTATION MODEL

A. Interatomic potential

The interatomic potentials play an important part in the molecular dynamics simulations since they govern the dynamics of the system and, thus the accuracy of the results. In this work, the following van der Waals type pair potential between At and Pt derived by Kulginov et al. [27] is used

TABLE I. Parameters of the Pt-Ar pairwise potential [27].

V_0 (eV)	α (Å^{-1})	R_0 (Å)	C_6 (eV.Å^6)
20000	3.3	-0.75	68.15

$$\phi_{Ar-Pt}(R_{Ar-Pt}) = V_0 e^{-\alpha(R_{Ar-Pt}-R_0)} - \frac{C_6}{R^6_{Ar-Pt}}, \quad R_{Ar-Pt} = |\mathbf{r}_{Ar} - \mathbf{r}_{Pt}| \quad (2)$$

where R_{Ar-Pt} is the distance between an Ar atom at location $\mathbf{r}_{Ar}$ and a Pt atom at location $\mathbf{r}_{Pt}$, or *vice versa*. Contrary to usual Lennard-Jones potentials, the repulsive part of this pair potential has a Born-Mayer form and provides a better description of the strong repulsion of the electrons. The pairwise potential parameters have been empirically adjusted such that the laterally average potential reproduces the measured properties of an Ar atom adsorbed on a slab of Pt atoms, i.e. a well depth of about 80 meV [28] and, a vibrational frequency of the adsorbed atom of about 5 meV [29]. The van der Waals interaction of an Ar atom with a platinum surface can be evaluated from the Ar-polarizability and the Pt-dielectric function. The values of the potential parameters are given in Table I and were shown to be in good agreement with an *ab-initio* based calculation [30]. In Ref. [30], the CRYSTAL09 software [31] was used to study the interaction between Ar and Pt(111) surface and results (e.g: equilibrium distance, potential well depth, etc..) are compared with several existing potentials for Ar/Pt.

In terms of the potential between the Pt atoms, the multi-body Quantum-Sutton Chen (QSC) potential is used [32]. As a particular Finnis-Sinclair potential type, the QSC potential includes quantum corrections and predict better temperature dependent properties. For a system of N Pt-atoms, the potential is given by the following expression

$$E_{pot,Pt} = \epsilon \left[\frac{1}{2} \sum_{i=1}^{N} \sum_{\substack{j=1 \\ j\neq i}}^{N} \left(\frac{a}{R_{ij}} \right)^n - c \sum_{i=1}^{N} \rho_i^{1/2} \right], \quad \rho_i = \sum_{\substack{j=1 \\ j\neq i}}^{N} \left(\frac{a}{R_{ij}} \right)^m \quad (3)$$

where a is the lattice constant, R_{ij} the distance between atom i and j and the local density ρ_i of atom i. The parameters ϵ and a determine the scales of energy and length, respectively and, n and m the range and shape of the potential. These potential parameters are

TABLE II. Quantum Sutton-Chen parameters for Pt [33].

n	m	ϵ (eV)	c	a (Å)
11	7	9.7894e-3	71.336	3.9163

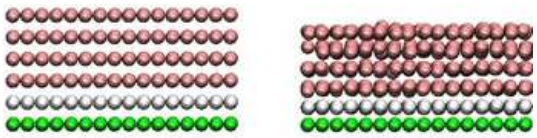

FIG. 1. (Color online) Surface effects: the fully relaxed configuration (right) is different from initial configuration (left). The solid film system is composed of fixed atoms (bottom layer), thermostat atom (upper bottom layer) and normal atoms (remaining layers).

given in Table II. Combining the Ar-Pt and Pt potentials, we can compute the total potential of the system

$$E_{pot} = \sum_{i=1}^{N} \phi_{Ar-Pt}(R_{Ar-i}) + E_{pot,Pt} \tag{4}$$

and the force $\mathbf{f}_i$ acting on atom i at position $\mathbf{r}_i$ by

$$\mathbf{f}_i = -\frac{\partial E_{pot}}{\partial \mathbf{r}_i} \tag{5}$$

Since we only consider the interaction of one Ar atom with a Pt surface, there is no contribution of the Ar-Ar term in the total potential formula E_{pot}. The accuracy of the QSC potential for Pt has been justified in Ref. [33] as it reproduces accurately the melting temperature and the specific heat of the material. Although its implementation is more costly than the harmonic (spring) potential, it should better reproduce the surface effects, since atoms near the free surfaces are different from the bulk. Our tests on the QSC potential show that in fully relaxed equilibrium system, the interatomic distance near the free surfaces is much smaller than in the bulk (see Fig. 1). As shown by previous works [34–36], the lattice constant, wall mass and stiffness can have significant impacts on σ and the slip effects.

B. Surface samples

In this paper, three types of surfaces are considered: smooth surfaces, periodic nanotextured surfaces and randomly rough surfaces. The orientation of their free surfaces is (100) according to the Miller index. Initially, the Pt atoms are arranged in layers and the two lowest ones (phantom atoms) are used to fix the system and for the thermostat purpose. The remaining Pt atoms are free to interact with other solid atoms and gas atoms.

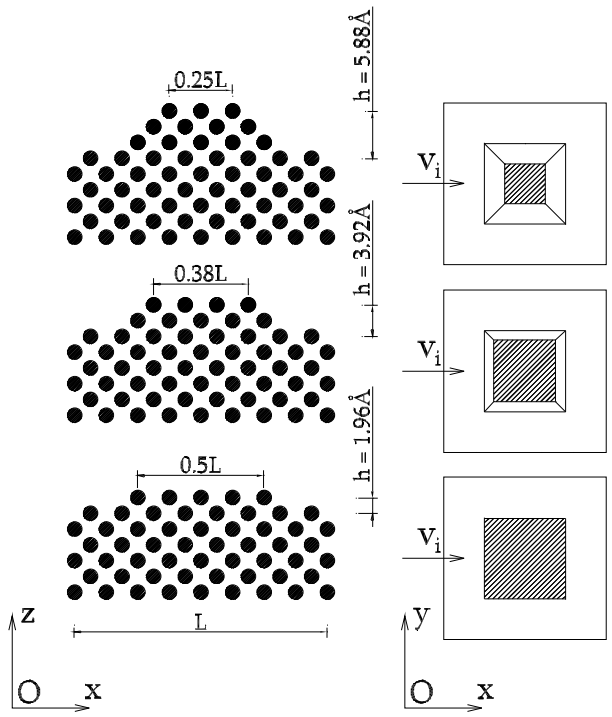

FIG. 2. Nanotextured surface of type A (square)

The random arrangement of these atoms defines the "rough" state of the surface and will be detailed later on.

A smooth surface model is a system composed of 768 atoms arranged in 6 layers, all of which are in perfect crystal order. The nanotextured models are constructed from the smooth surface model by adding successively atom layers to create pyramids with the slope angle 45°. The slope is necessary to assure the stability of the system since perfectly vertical blocks (slope angle 90°) are less stable: in many cases atoms migrate to lower positions and the blocks evolve into step-like structures with smaller potential energy. The base of the pyramid can be a square (type A, Fig. 2) or an infinite strip (type B, Fig. 3), so that both isotropic/anisotropic effect can be considered. Although these pyramids are simplified models of a real rough surface, it can show the dependence of σ on the roughness. The latter in MEMS/NEMS is reported to be several Å [1]. In this work, the highest peak, varying with the number of atoms layers added on the surfaces, ranges from 2 to 6 Å.

Randomly rough surface models are also constructed by adding atoms on the smooth surfaces in a random way. In the available literature, there are several mathematical models [37–40] that describe random roughness. However, these models are not suitable at atomic scale: it is difficult to force atoms to be at given positions

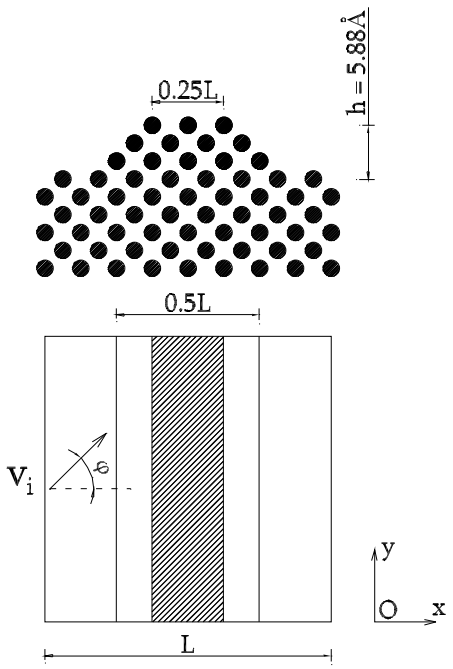

FIG. 3. Nanotextured surface of type B (strip)

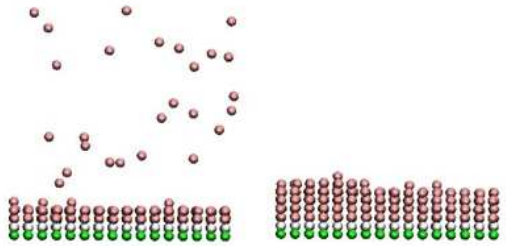

FIG. 4. (Color online) Snapshot of deposition process (left) and final thin film system (right)

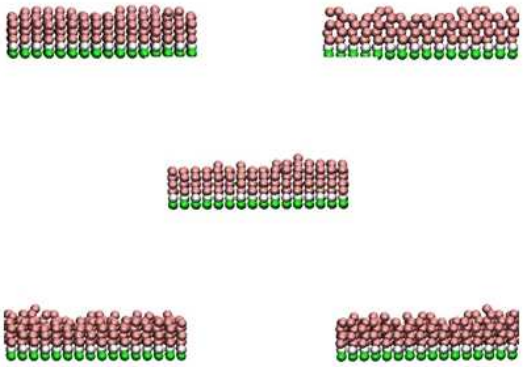

FIG. 5. (Color online) Five samples obtained from the deposition process

and, structure parameters such as orientation (100) and lattice constant must be respected. Furthermore such atomistic systems might not be appropriate in terms of potential energy. In our opinion, a randomly rough surface which is consistent with the internal atomistic structure, should be built from molecular dynamics simulations. Rapid cooling of thin films from the liquid state [41] can create rough surfaces but the final systems could contain many defects (e.g. pores, dislocations) and non crystalline structure. As the paper focuses on Pt (100), the rough surfaces are constructed by deposing atoms randomly on the existing smooth Platinum surface. Since this procedure is quite similar to the film vapor-deposition processes, it is asssumed that the created surface is quite close to real MEMS/NEMS surfaces. The procedure of the material deposition is described as follows. The initial system is a Pt plate made of four layers of 512 solid atoms, arranged in (100) fcc order. First, the system is relaxed towards the minimal potential energy configuration. Then, after 2000 time steps of 1 fs, a Pt atom is inserted randomly from a height of 10 Å with the initial thermal velocity corresponding to 1000 K. Under the attraction force (QSC potential) from the Pt plate, the deposed Pt atoms move downwards until they reach the plate which is maintained at 50 K. (see a snapshot of the deposition process in Fig. 4). Finally, when all inserted Pt atoms are attached firmly into the Pt plate, the whole system undergoes the anneal process at the ambient temperature $T_a = 300$ K with a time step equal to 2 fs. During the whole simulation, the Leap-Frog Verlet integration scheme is employed and the temperature is kept constant by simple velocity scaling method. Figure 4 shows a snapshot of the final system whose total number of Pt atoms have reached 733. To improve the statistical results, 5 samples obtained thanks to the above described procedure are collected, as shown in Fig. 5.

C. Dynamics of gas/wall collision

In what follows, we describe the MD method used to simulate the gas-wall collision and to calculate the σ coefficient. The simulations are three dimensional: an Ar atom is projected into a Pt(100) surface with different incident angles θ and with different approaching φ-planes. In spherical coordinate system, (θ, φ) are the polar and azimuthal angles, respectively (see Fig 6). The *directional* σ_{dir} coefficient associated with each θ and φ is defined by the following formula [1]:

$$\sigma_{dir}(\theta, \varphi) = \frac{\langle v_{in} \rangle - \langle v_{rn} \rangle}{\langle v_{in} \rangle}, \tag{6}$$

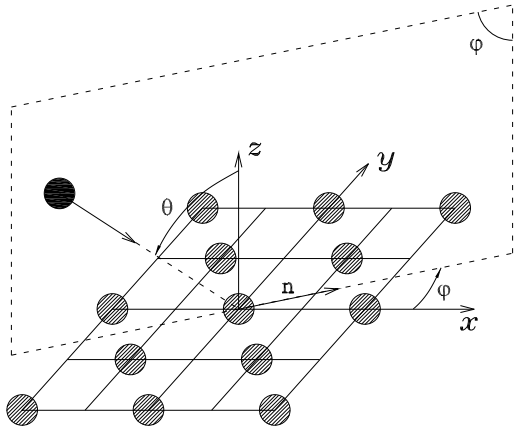

FIG. 6. Representation of θ, φ in cartesian coordinate system

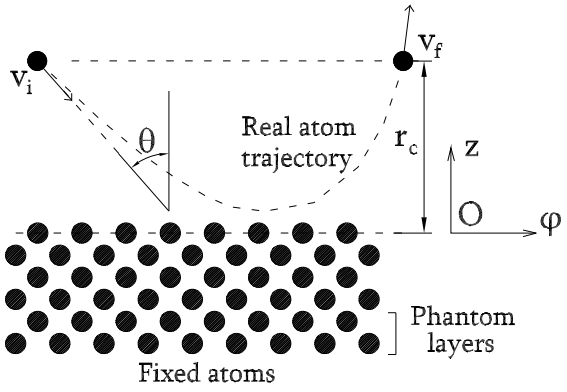

FIG. 7. Molecular dynamics scheme. The incident argon atoms are with v_i velocities. θ is the incident angle. The Pt wall has a fcc structure with a (100) surface. The Pt atoms are controlled by Sutton-Chen potential.

where v_{in} and v_{rn} are the projections of the incident and the reflected velocity on the vector $\mathbf{n}$, respectively. The latter is the intersection of the plane xOy and the φ-plane, i.e it lies on xOy and makes an angle φ with respect to Ox. Only one gas-wall collision is treated per simulation and the averages $\langle v_{in}\rangle, \langle v_{rn}\rangle$ in Eq. (6) are taken over a large number of simulations (or collisions). The definition (6) is the most accurate description of gas-wall interaction since it is associated to each direction. We also calculate the *effective anisotropic* $\sigma_{an}(\varphi)$ coefficients using the same equation (6) but with gas atoms arriving from all directions: the direction of $\mathbf{v}_i$ is randomly uniform with $v_{in} > 0$. In the special case where the surface is isotropic, σ_{an} varies little with φ and a single *effective isotropic* σ_{iso} constant is sufficient for modelling gas-wall interaction as in Maxwell's model. The latter *effective isotropic* coefficient is obtained by the similar method but $\langle v_{in}\rangle, \langle v_{rn}\rangle$ in Eq. (6) are further averaged over $\mathbf{n}$ (or φ).

We assume first that an Ar atom only interacts with the Pt wall within a cutoff distance $r_c = 10$ Å. Since this distance is much smaller than the typical mean free path at atmospheric pressure or in high vacuum ($\lambda > 69$ nm), it can justify the choice of such a small region to calculate the σ coefficients. At a distance of 10 Å, an Ar atom can be considered as non-interacting with the Pt-wall atoms since the potential value at that distance (-0.0580736meV) is negligibly small when compared with the potential well depth (10.21 meV). At the beginning of each simulation, an Ar atom is inserted randomly at the height r_c above the wall surface with initial incident velocity $\mathbf{v}_i$. The norm of $\mathbf{v}_i$ is equal to the thermal speed corresponding to the gas beam temperature T_g. Although the results of this work are obtained using a constant incident velocity corresponding to the gas temperature, we have done separate simulations using the Maxwell-Boltzmann velocity distribution and find that σ is insensitive to this modification. A collision is considered as finished when the atom bounces back beyond the cutoff distance. Then the reflected velocity $\mathbf{v}_r$ is recorded for the statistical purpose and another Ar atom is reinserted randomly to continue the process. After approximatively 10000 collisions (simulations), converged values of σ values were obtained. Numerical tests show that the statistical error of a typical 10000-collision average is within 1.0%.

Throughout the simulations, periodic boundary conditions were applied along the x, y directions. The velocities and positions of gas atoms and the solid atoms at each time step are calculated by the usual Leap-Frog Verlet integration scheme. To control the temperature T_w of the system, the phantom technique is used: the Langevin thermostat [42] is applied to the atom layer above the fixed layers. The motion of an atom i belonging to this layer is governed by the equation

$$m_i \frac{d\mathbf{v}_i(t)}{dt} = -\xi \mathbf{v}_i(t) + \mathbf{f}_i(t) + \mathbf{R}_i(t). \qquad (7)$$

In Eq. (7), $\mathbf{v}_i$ is the velocity of the atom i, $\mathbf{f}_i$ is the resulting force acting on it by the surrounding ones, m_i is the atomic mass and ξ is the damping coefficient. The third term $\mathbf{R}_i$ in the right hand side of Eq. (7) is the random force applied on the atom. In the simulation, it is sampled after every time step δt from a Gaussian distribution with zero average and mean deviation of $\sqrt{6\xi k_B T_w/\delta t}$. The simulations were carried out by setting time step and damping factor at the following values:

$$\delta t = 2 \text{ fs}, \quad \xi = 5.184 \times 10^{-12} \text{kg/s}. \qquad (8)$$

The wall temperature T_w was kept at 200 K, 300 K and 400 K and the gas beam temperature T_g was kept at a slightly higher value than T_w, here $T_g = 1.1T_w$. Such choice of T_g was made arbitrarily and the procedure of the present work can be applied to any gas temperature. Generally, to obtain the best statistical results, a typical

TABLE III. $\sigma_{dir}(\theta, \varphi)$ computed at $T_w = 200\ K$, $300\ K$, $400\ K$ for three roughness heights h with $\theta = 10°$, $45°$, $80°$ and $\varphi = 0°$.

Surface type	θ	$T_w = 200\ K$	$T_w = 300\ K$	$T_w = 400\ K$
A (h =5.88 Å)	10°	0.96	0.87	0.79
	45°	0.92	0.85	0.77
	80°	0.90	0.83	0.74
A (h =3.92 Å)	10°	0.94	0.84	0.75
	45°	0.90	0.79	0.74
	80°	0.88	0.78	0.72
Smooth	10°	0.85	0.72	0.61
	45°	0.82	0.70	0.60
	80°	0.80	0.69	0.59

run requires 4×10^7 time steps of 2 fs. All simulations were run on 9 processors, using a domain decomposition and the Message Passing Interface. The longest simulation takes about 20 CPU hours. We have carried out computations with different time steps from 1fs to 3fs and we have found that the results are insensitive to this factor.

III. MD SIMULATION RESULTS

A. Effects of temperature and roughness height

From the description of the models in Section 2, the coefficient σ_{dir} can depend on the several input parameters: temperature, surface morphology, incident direction (θ, φ). The variation of σ_{dir} in terms of these parameters is investigated in the following subsections.

The σ_{dir} results at different temperatures are shown in Tables III and Fig. 8. A general trend can be noticed here: σ_{dir} increases as the temperature decreases, ranging from 0.78 to 0.92 in the case of the highest roughness considered ($h = 5.88$ Å). This trend in σ_{dir} variation can be explained by the fact that the adsorption is stronger with colder walls. Gas atoms stay longer near the wall, interact more with solid atoms and, as a result, the reflection is more diffusive. Similar remarks have been reported in Refs. [6, 43] for confined systems. For $h = 5.88$ Å and $T_w = 300\ K$, Table IV shows that the σ_{dir} value varies very little with the incident angle θ and very close to the average isotropic value $\sigma_{iso} = 0.85$. This means that for this kind of surface, Maxwell's one parameter model is sufficiently accurate to model gas-wall interaction.

The σ_{dir} coefficient increases with the roughness of the wall surface (see Table III and Fig. 8). Computations carried out for pyramidal structures at the temperature of 300 K show that the σ_{dir} coefficient can reach up to 0.87 for surfaces with the highest peak configuration. It

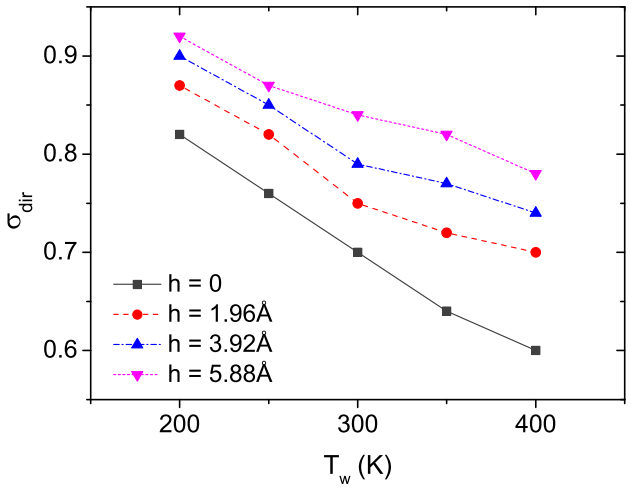

FIG. 8. (Color online) σ_{dir} computed for the wall of type A (square) at $T_w = 200\ K$, $250\ K$, $300\ K$, $350\ K$ and $400\ K$ for three roughness heights h with $\theta = 45°$ and $\varphi = 0°$.

TABLE IV. σ_{iso} and $\sigma_{dir}(\theta, \varphi)$ computed at $T_w = 300\ K$.

Surface type	φ	θ	σ_{dir}	σ_{iso}
A (h =5.88 Å)	0°	10°	0.87	–
	0°	30°	0.86	–
	0°	45°	0.85	–
	0°	60°	0.85	–
	0°	80°	0.83	–
	–	–	–	0.85
Random (Fig. 5)	–	–	–	0.92
Smooth	–	–	–	0.70

is clear that the presence of peaks leads to non uniform surface potentials with local minima where gas molecules can easily be trapped: the gas atoms stays longer near the wall, interact more with it and lose their initial momentum. Moreover, the changes in local slopes produce more or less random variations in the local incident and reflection angles. Visualization of collision trajectories shows a clear difference between a smooth surface and a rough surface. On a smooth surface, a gas molecule collides and bounces several times before finally escaping from the influence distance r_c of the wall (see Fig. 9). On a rough surface, it stays near the wall and moves around the valley between the peaks, a mechanism similar to surface diffusion, until the wall provides enough energy to escape (see Fig. 10). Although the real behaviors are mixed: we sometimes observe the colliding/bouncing mechanism on rough surfaces and vice versa (not shown in Figs. 9,10) but they are not typical.

Next we considered the case of random surfaces ob-

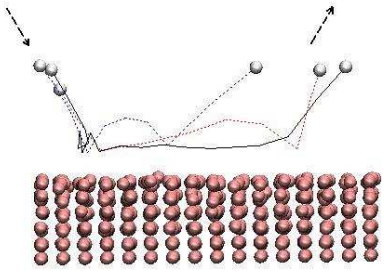

FIG. 9. (Color online) Typical collision trajectories (solid and dashed lines) on a smooth surface. Gas molecules collide and bounce several times before escaping.

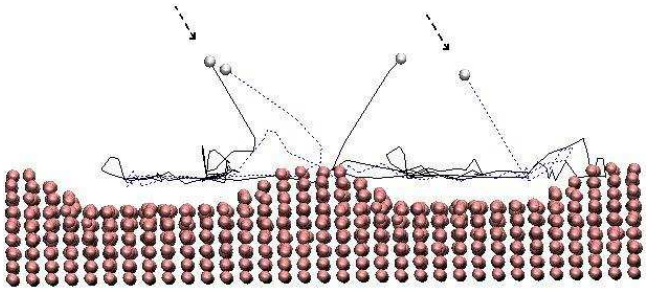

FIG. 10. (Color online) Typical collision trajectories (solid and dashed lines) on a rough surface. Gas molecules move around in the valley between the peaks.

tained from the atom deposition process. With the same parameters for the deposition process, the σ_{dir} obtained for the five samples shown in Fig. 5 exhibit small differences, from 0.90 to 0.93. It is very close to σ_{iso} value for random surfaces 0.92 (see Table IV). Thus, in addition to the roughness height, the in-plane random arrangement of the atoms also plays a significant role on the accommodation coefficient.

B. Surface anisotropy effect

An anisotropic textured surface can obstruct or facilitate the flows differently along different directions. Bazant and Vinogradova [18] generalized Navier slip boundary conditions for anisotropic texture surface by using a tensorial slip length. In the framework of the kinetic theory, Dadzie and Meolans [24] proposed a new scattering kernel that accounts for surface anisotropy. Their formulation is based on three independent accommodation coefficients $\alpha_x, \alpha_y, \alpha_z$ along the three directions x, y, z. The coefficients α_x, α_y represent the tangential accommodation coefficients and α_z is the normal accommodation coefficient. The tangential accommodation coefficient α_n in direction n is then computed by the expression (see Appendix A)

$$\sigma_{an}(\varphi) = \alpha_n = \alpha_x \cos^2\varphi + \alpha_y \sin^2\varphi \qquad (9)$$

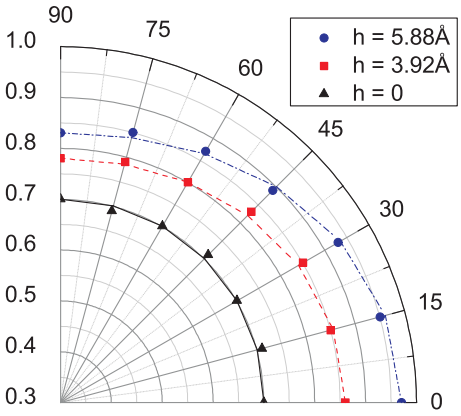

FIG. 11. (Color online) σ_{dir} computed for type-B walls (strip) versus azimuth angle φ for different roughnesses ($T_w = 300K$, $\theta = 45°$).The solid, dashed, dash-dotted lines are the analytical expressions (9) used to fit the present numerical results.

We remark that by substituting $\varphi = 0°$ and $\varphi = 90°$, the accommodation values α_x and α_y along x, y direction can be recovered. In this subsection, we study the anisotropy effect using MD and the directional σ definition in Eq. (6) and examine the relation (9). The anisotropy effect can be seen from Figs. 11 and 12: the σ_{dir} variation with φ is non uniform for rough surfaces. The accommodation process along the two directions x, y is highly different. The σ_{dir} is minimum when the atoms are projected along the longitudinal direction of the strip ($\varphi = 90°$), since the surface may be considered as almost smooth in that direction (see Fig. 3). This σ value corresponds to α_y in the model of [24]. The maximal σ values recorded for $\varphi = 0°$ and $h > 0$ can be attributed to the largest roughness effect in that direction and correspond to α_x in the model [24]. Moreover, Figs. 11 and 12 show an increase of anisotropy effect as the roughness increases: the difference between the highest and the smallest σ value increases with the roughness height whereas the σ results depend very little on the beaming direction for a smooth surface. This could be explained by the fact that the smooth surface can be considered isotropic. Although Figs. 11 and 12 show discrepancies of σ obtained in different ways, all curves can fit reasonably well the analytical relation (9).

For anisotropic surfaces, the reflected flux is not always lying in the same plane with the arriving one. Consequently, in addition to Eq. (6), we should account for the ratio of the reflected flux components along two orthogonal directions m, n: $\langle v_{rm}\rangle/\langle v_{rn}\rangle$. According to the anisotropic model (see Appendix A), this ratio can be computed by the expression

$$\langle v_{rm}\rangle/\langle v_{rn}\rangle = \frac{(\alpha_x - \alpha_y)\cos\varphi\sin\varphi}{1 - \alpha_x\cos^2\varphi - \alpha_y\sin^2\varphi}. \qquad (10)$$

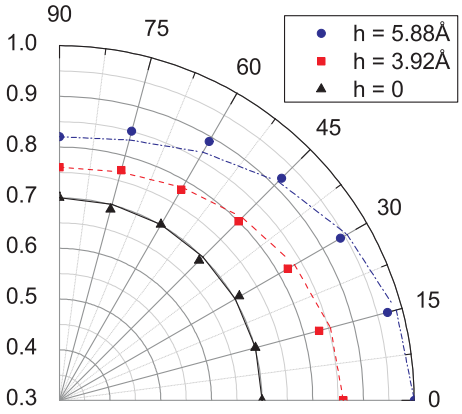

FIG. 12. (Color online) σ_{an} computed for type-B walls (strip) versus azimuth angle for different roughnesses ($T_w = 300K$). The solid, dashed, dash-dotted lines are the analytical expressions (9) used to fit the present numerical results.

TABLE V. Ratio $\langle v_{rm}\rangle/\langle v_{rn}\rangle$ computed for type-B walls (strip) with different roughness heights h at $T_w = 300K$, $\theta = 45°$ and $\varphi = 45°$.

h	$\langle v_{rm}\rangle/\langle v_{rn}\rangle$
0	0
1.96 Å	0.15
3.92 Å	0.39
5.88 Å	0.67

By observing the surface structure, we can deduce that $\langle v_{rm}\rangle/\langle v_{rn}\rangle$ must vanish for impinging fluxes parallel to the planes of symmetry of the anisotropic surface. That remark is in good agreement with Eq. (10) where $\langle v_{rm}\rangle/\langle v_{rn}\rangle = 0$ at $\varphi = 0°, 90°$. Our MD simulation confirms the remark and also shows that the ratio is nonzero at $\varphi \neq 0$. From Table V, at $\varphi = 45°$, we find that the ratio is significant. It even increases with the roughness height increases, i.e the anisotropic effect is enhanced.

IV. CONCLUDING REMARKS

In this paper, we have studied the effects of temperature, surface textures and anisotropy on the σ coefficient. The computation model is based on the molecular beam experiments and constructed with the accurate available potentials and interaction models. Although σ is not a simply gas/wall constant, the MD result range agrees quite well with the experimental range at the ambient temperature. The randomly rough surface obtained from the atomic deposition simulation is also investigated in the paper.
Concerning the anisotropy effect, results on systems with anisotropic surfaces show that σ varies significantly with orientation. Effective σ coefficients are obtained and compared with the available model in the literature.

Appendix A: Anisotropic scattering kernel

For gas-wall interaction, Dadzie and Meolans [24] proposed an anisotropic scattering kernel $B(\mathbf{v}', \mathbf{v})$ defined by

$$B(\mathbf{v}', \mathbf{v}) = \sum_k \mu_k B_k(\mathbf{v}', \mathbf{v}) \tag{A1}$$

in which

$$\begin{aligned} \mu_{ij} = \alpha_i\alpha_j(1-\alpha_k), \quad \mu_i = \alpha_i(1-\alpha_j)(1-\alpha_k), \\ \mu_{ijk} = \alpha_i\alpha_j\alpha_k, \\ \mu_0 = (1-\alpha_i)(1-\alpha_j)(1-\alpha_k), \quad i,j,k = x,y,z, \\ i \neq j \neq k \neq i. \end{aligned} \tag{A2}$$

The vectors $\mathbf{v}', \mathbf{v}$ are respectively the arriving velocity and the reflected one and the constants $\alpha_x, \alpha_y, \alpha_z$ are the accommodation coefficients along the directions x, y, z. The elementary kernels B_k are given by the following expressions

$$\begin{aligned} B_0(\mathbf{v}', \mathbf{v}) &= \delta(v_z + v_z')\delta(v_x - v_x')\delta(v_y - v_y') \\ B_{xy}(\mathbf{v}', \mathbf{v}) &= \frac{1}{\pi C_w^2}\delta(v_z + v_z')e^{-(v_y^2+v_x^2)/C_w^2} \\ B_{iz}(\mathbf{v}', \mathbf{v}) &= \frac{2}{\sqrt{\pi}C_w^3}v_z\delta(v_j - v_j')e^{-(v_i^2+v_z^2)/C_w^2} \\ B_{xyz}(\mathbf{v}', \mathbf{v}) &= \frac{2}{\pi C_w^4}v_z e^{-(v_x^2+v_y^2+v_z^2)/C_w^2} \\ B_i(\mathbf{v}', \mathbf{v}) &= \frac{1}{\sqrt{\pi}C_w}\delta(v_z + v_z')\delta(v_j - v_j')e^{-v_i^2/C_w^2} \\ B_z(\mathbf{v}', \mathbf{v}) &= \frac{2}{C_w^2}v_z\delta(v_i - v_i')\delta(v_j - v_j')e^{-v_z^2/C_w^2}, \\ & \qquad i,j = x,y, \quad i \neq j. \end{aligned} \tag{A3}$$

where δ is the delta Dirac and C_w is a velocity constant depending on the wall temperature. The boundary conditions for particle distribution function $f(\mathbf{v})$ is then defined by

$$\begin{aligned} v_z f(\mathbf{v}) = \int_{\Omega'} |v_z'| f(\mathbf{v}') B(\mathbf{v}', \mathbf{v}) d\mathbf{v}', \\ \Omega' = \mathbb{R} \times \mathbb{R} \times \mathbb{R}^- \end{aligned} \tag{A4}$$

We use Φ_j^- and Φ_j^+ to denote the incoming flux at the wall of the momentum j component. Then

$$\begin{aligned} \Phi_j^- = \int_{\Omega'} m|v_z'|v_j' f^-(\mathbf{v}')d\mathbf{v}', \quad \Phi_j^+ = \int_{\Omega} m|v_z|v_j f^+(\mathbf{v})d\mathbf{v}, \\ \Omega' = \mathbb{R} \times \mathbb{R} \times \mathbb{R}^+. \end{aligned} \tag{A5}$$

with f^- and f^+ being the velocity distribution associated with the incident molecules and reflected molecules. Dadzie and Meolans [24] proved the following relation

$$\frac{\Phi_j^- - \Phi_j^+}{\Phi_j^-} = \alpha_j, \quad j = x, y, z. \tag{A6}$$

Their model is based on three parameters $\alpha_x, \alpha_y, \alpha_z$ defined along given directions of a system of coordinate. We are interested in the accommodation coefficients in an arbitrary direction. Hence, we consider a family of orthogonal directions $(\mathbf{n}, \mathbf{m})$ obtained by rotating xOy around Oz by an angle φ. Consequently, the n, m-components are related to x, y components by

$$\Phi_n^\pm = \cos\varphi\Phi_x^\pm + \sin\varphi\Phi_y^\pm, \quad \Phi_m^\pm = -\sin\varphi\Phi_x^\pm + \cos\varphi\Phi_y^\pm \tag{A7}$$

Since α_x and α_y are accommodation coefficients, we can deduce the the relation

$$\begin{aligned} \Phi_n^+ &= (1-\alpha_n)\Phi_n^- + \beta_{nm}\Phi_m^-, \\ \Phi_m^+ &= (1-\alpha_m)\Phi_m^- + \beta_{nm}\Phi_n^-, \end{aligned} \tag{A8}$$

with

$$\begin{aligned} \beta_{nm} &= (\alpha_x - \alpha_y)\cos\varphi\sin\varphi, \\ \alpha_n &= \alpha_x\cos^2\varphi + \alpha_y\sin^2\varphi, \\ \alpha_m &= \alpha_y\cos^2\varphi + \alpha_x\sin^2\varphi, \end{aligned} \tag{A9}$$

and compute the accommodation coefficient along any direction n. For example, by setting the component $\Phi_m^- = 0$ (e.g we beam atoms along direction n only), we can recover the expression for α_n in Eq. (9). The ratio between the reflected components m, n can also be computed by the expression

$$\Phi_m^+/\Phi_n^+ = \frac{\beta_{nm}}{1-\alpha_n} = \frac{(\alpha_x - \alpha_y)\cos\varphi\sin\varphi}{1 - \alpha_x\cos^2\varphi - \alpha_y\sin^2\varphi}. \tag{A10}$$

It is clear that for isotropic model $\alpha_x = \alpha_y$, this ratio is always zero for all φ. Thus for anisotropic surface $\alpha_x \neq \alpha_y$, the ratio Φ_m^+/Φ_n^+ is a function of φ, only vanishes at $\varphi = 0°, 90°$. For example, at $\varphi = 45°$, we obtain

$$\Phi_m^+/\Phi_n^+ = \frac{\alpha_x - \alpha_y}{2 - \alpha_x - \alpha_y}. \tag{A11}$$

[1] G. Karniadakis, A. Beskok, and N. Aluru, *Microflows and Nanoflows: Fundamentals and Simulation* (Springer, New York, 2005).
[2] J. C. Maxwell, Philos. T. Roy. Soc. London **170**, 231 (1879).
[3] B. Y. Cao, J. Sun, M. Chen, and Z. Y. Guo, Int. J. Mol. Sci. **10**, 4638 (2009).
[4] E. B. Arkilic, K. S. Breuer, and M. A. Schmidt, J. Fluid Mech. **437**, 29 (2001).
[5] Q. D. To, C. Bercegeay, G. Lauriat, C. Léonard, and G. Bonnet, Microfluid. Nanofluid. **8**, 417 (2010).
[6] B. Y. Cao, M. Chen, and Z. Y. Guo, Appl. Phys. Lett. **86**, 091905 (2005).
[7] Q. D. To, T. T. Pham, G. Lauriat, and C. Léonard, Adv. Mech. Eng. **2012** (2012).
[8] D. Rapaport, *The Art of Molecular Dynamics Simulation* (Cambridge University Press, 2004).
[9] M. Allen and D. Tildesley, *Computer Simulation of Liquids* (Oxford University Press, 1989).
[10] G. W. Finger, J. S. Kapat, and A. Bhattacharya, J. Fluid. Eng. **129**, 31 (2007).
[11] C. T. Rettner, IEEE T. Magn. **34**, 2387 (1998).
[12] G. Bird, *Molecular Gas Dynamics and the Direct Simulation of Gas Flows* (Clarendon Press, 1994).
[13] W. Liou and Y. Fang, *Microfluid Mechanics* (McGraw-Hill, 2003).
[14] H. Struchtrup, *Macroscopic Transport Equations for Rarefied Gas Flows: Approximation Methods in Kinetic Theory* (Springer, 2005).
[15] M. Kalweit and D. Drikakis, J. Comput. Theor. Nanos. **5**, 1923 (2008).
[16] M. Kalweit and D. Drikakis, Proc. IMech E Part C J. Mech. Eng. Sci. **222**, 797 (2008).
[17] M. Kalweit and D. Drikakis, Mol. Simulat. **36**, 657 (2010).
[18] M. Z. Bazant and O. I. Vinogradova, J. Fluid. Mech. **613**, 125 (2008).
[19] N. V. Priezjev, J. Chem. Phys. **135**, 204704 (2011).
[20] L. Bocquet and J. L. Barrat, Phys. Rev. E **49**, 3079 (1994).
[21] L. Bocquet and J. L. Barrat, Soft Matter **3**, 685 (2007).
[22] F. Feuillebois, M. Z. Bazant, and O. I. Vinogradova, Phys. Rev. Lett **102**, 026001 (2009).
[23] F. Feuillebois, M. Z. Bazant, and O. I. Vinogradova, Phys. Rev. E **82**, 055301 (2010).
[24] S. K. Dadzie and J. G. Meolans, J. Math. Phys. **45**, 1804 (2004).
[25] The source code is available for download at http://www.ph.biu.ac.il/∼rapaport/mdbook.
[26] W. Humphrey, A. Dalke, and K. Schulten, J. Molec. Graphics **14**, 33 (1996).
[27] D. Kulginov, M. Persson, C. T. Rettner, and D. S. Bethune, J. Chem. Phys. **100**, 7919 (1996).
[28] M. Head-Gordon, J. C. Tully, C. T. Rettner, C. B. Mullins, and D. Auerbach, J. Chem. Phys. **94**, 1516 (1991).
[29] P. Zeppenfeld, U. Becher, K. Kern, R. David, and G. Comsa, Phys. Rev. B **41**, 8549 (1990).

[30] C. Léonard, V. Brites, T. T. Pham, Q. D. To, and G. Lauriat, submitted to Eur. Phys. J. B (2012).
[31] R. Dovesi, R. Orlando, B. Civalleri, C. Roetti, V. Saunders, and C. Zicovich-Wilson, Z. Kristallogr. **220**, 571 (2005).
[32] A. P. Sutton and J. Chen, Philos. Mag. Lett. **61**, 139 (1990).
[33] S. K. R. S. Sankaranarayanan, V. R. Bhethanabotla, and B. Joseph, Phys. Rev. B **74**, 155441 (2006).
[34] G. Arya, H.-C. Chang, and E. J. Maginn, Mol. Simulat. **29**, 697 (2003).
[35] N. Asproulis and D. Drikakis, Phys. Rev. E **84**, 031504 (2011).
[36] N. Asproulis and D. Drikakis, Phys. Rev. E **81**, 061503 (2010).
[37] B. Bhushan, *Modern Tribology Handbook*, Vol. 1 (CRC, 2001).
[38] A. Majumdar and B. Bhushan, J. Tribol. T. ASME **112**, 205 (1990).
[39] B. Mandelbrot, *The Fractal Geometry of Nature* (Wh Freeman, 1983).
[40] B. B. Mandelbrot, D. E. Passoja, and A. J. Paullay, Nature **308**, 721 (1984).
[41] V. V. Hoang and T. Q. Dong, Phys. Rev. B **84**, 174204 (2011).
[42] T. Schlick, *Molecular Modeling and Simulation: an Interdisciplinary Guide* (Springer Verlag, 2010).
[43] P. Spijker, A. J. Markvoort, S. V. Nedea, and P. A. J. Hilbers, Phys. Rev. E **81**, 011203 (2010).